



Heat transfer enhancement in microchannel heat sink with bidirectional rib

Guilian Wang^{a,*}, Nan Qian^a, Guifu Ding^b

^a School of Electronic and Electrical Engineering, Shanghai University of Engineering Science, 333 Longteng Road, Shanghai 201620, People's Republic of China

^b National Key Laboratory of Science and Technology on Micro/Nano Fabrication, Shanghai Jiao Tong University, Shanghai 200240, People's Republic of China

ARTICLE INFO

Article history:

Received 10 September 2018

Received in revised form 25 January 2019

Accepted 9 February 2019

Keywords:

Bidirectional rib

Microchannel

Heat transfer

Pressure drop

ABSTRACT

The heat transfer and flow characteristics of the microchannel heat sink (MCHS) with bidirectional ribs (BRs) are experimentally and numerically studied in the present paper. The BR, composed of vertical rib (VR) and spanwise rib (SR), can interrupt the thermal boundary layer and induce recirculation in both vertical and spanwise directions. Its cooling effectiveness is compared with that of the widely-used VR and SR for the Reynolds number ranged from 100 to 1000. The results show that the Nusselt number of the microchannel with BRs (BR-MC) is up to 1.4–2 and 1.2–1.42 times those of microchannels with VRs (VR-MC) and SRs (SR-MC), respectively. This implies that the BR can strengthen the heat transfer more sufficiently. Meanwhile, the utilizing of BR gives rise to the larger pressure drop penalty due to its broader obstruction areas. In addition, the higher relative rib height of VR (e_{VR}) and relative rib width of SR (e_{SR}) are revealed to enhance the heat transfer but induce pressure drop in the BR-MC. The thermal enhancement factor can keep larger than 1 when $e_{VR} < 0.316$ and $0.026 < e_{SR} < 0.357$.

© 2019 Published by Elsevier Ltd.

1. Introduction

The inexorable miniaturization and high speed operation of electronic devices have resulted in a tremendous increase in power density, which will cause huge amount of heat in electronic devices. To avoid heat accumulation and preserve their component lifespan and reliability, many powerful heat dissipation methods have been developed till now which include microchannel heat sink (MCHS), jet impingement, sprays, heat pipes, piezoelectrically driven droplets, etc. [1–5]. Among these techniques, MCHS is the most practical choice due to its favorable and attractive features such as light weight, compactness and high heat transfer area to volume ratio [6–11]. The water-cooled microchannel technology was proposed initiatively by Tuckerman and Pease [12]. They demonstrated that a heat flux as high as 790 W/cm^2 can be removed with a maximum substrate temperature rise of $71 \text{ }^\circ\text{C}$.

Although high thermal performance can be achieved by using MCHS, several techniques, such as nanofluid, surface area increase and thermal boundary layer redeveloping, have been proposed to promote the heat transfer with the escalating thermal demands of electronic devices. Arani et al. [13] numerically investigated water/single-wall carbon nanotubes nanofluid in a double layered MCHS. They concluded that the increase of nanoparticle volume

fraction causes an increment of the Nusselt number but pressure drop augmentation. Hung et al. [14] investigated the hydraulic and thermal performances of the porous-MCHSs with different configuration designs. They found that porous microchannels can improve the cooling performance due to the surface area increase. Xu et al. [15] studied experimentally and numerically the hydrothermal characteristics of silicon MCHS which consists of ten parallel triangular microchannels separated by five transverse trapezoidal microchannels. They found that the proposed MCHS can decrease the temperature by $14 \text{ }^\circ\text{C}$ compared with the conventional MCHS. The results demonstrated that the redeveloping of thermal boundary layer has a significant effect on improving the heat transfer in the MCHS.

Based on the thermal boundary layer redeveloping mechanism, some researchers proposed the MCHS with variable cross-sections, fins, grooves or ribs. Chai et al. [16] numerically and experimentally investigated the fluid flow and heat transfer in MCHS with periodic expansion–contraction cross-sections. The results show that the expansion–contraction cross-sections provide a significant influence on the heat transfer. Shafeie et al. [17] performed detailed numerical study of the MCHS with different height of micro pin fins. It was shown that the finned microchannels have better heat transfer performance than the smooth microchannels at the same pumping power. Moreover, the finned case with highest fin depth (500 μm) had the highest heat removal among studied finned heat sinks. Ahmed et al. [18] investigated numerically

* Corresponding author.

E-mail address: wglwrc2016@126.com (G. Wang).

Nomenclature

A	area, m^2	\bar{u}	mean flow velocity, m s^{-1}
C_p	specific heat, $\text{J kg}^{-1} \text{K}^{-1}$	w	width, m
D_h	hydrodynamic diameter, m		
f	frictional factor	<i>Greek symbols</i>	
h	heat transfer coefficient, $\text{W m}^{-2} \text{K}^{-1}$	μ	dynamic viscosity, Pa s
l	length, m	ρ	density, kg m^{-3}
\dot{m}	mass flow rate, kg s^{-1}	λ	thermal conductivity, $\text{W m}^{-1} \text{K}^{-1}$
N	the number of microchannels in heat sink		
Nu	Nusselt number	<i>Subscripts</i>	
P	pitch of the rib, m	c	microchannel
p	pressure, Pa	f	fluid
Q	total heat transfer, W	in	inlet
q	heat flux, W m^{-2}	out	outlet
ΔT	temperature difference, K	r	rib
T	temperature, K	s	smooth microchannel
t	thickness, m	w	wall
u	velocity, m s^{-1}		

the MCHS with triangular, trapezoidal and rectangular grooves. They found that there was a significant enhancement in heat transfer using grooved microchannels, and the ones with trapezoidal groove can provide the highest Nusselt number enhancement of 51.59%.

The ribs, also called roughness elements or turbulators, have been extensively studied and widely used due to their marked effect on the heat transfer enhancement. Chai et al. [19] investigated the pressure drop and heat transfer characteristics of the interrupted MCHS with rectangular ribs. Compared with interrupted microchannel without rectangular ribs and smooth microchannel, the interrupted one with rectangular ribs can provide the higher heat transfer enhancement factor. Desrues et al. [20] conducted numerical simulations to study the thermal performance of the microchannels with alternated vertical ribs and found that the proposed microchannels with VRs can provide a higher Nusselt number than the smooth ones. Jiang et al. [21] carried out experimental and numerical studies to investigate the flow and heat transfer characteristics of mist/steam two-phase flow in the channel with 60 deg spanwise ribs. They showed that ribs mounted on the sidewalls could lead to secondary flows and then improved the heat transfer characteristics. Xie et al. [22] performed an experimental study for heat transfer enhancement in a MCHS with various vertical crescent ribs protruded from the bottom wall. It was found that the ribs can improve the heat transfer performance by generating vortices. Xia et al. [23] computationally investigated the hydrothermal performance of MCHS with spanwise cavities and ribs. The results showed that Nusselt number for the MCHS with spanwise cavities and ribs increased about 1.3–3 times more than the rectangular microchannel, while the apparent friction factor increased about 6.5 times more.

Although thermal performance enhancement in MCHS can be achieved by using ribs, high pressure drop is also induced due to high-flow disturbances and blocking-flow effect. Therefore, the geometry and arrangement of ribs should be optimized to trade-off between the enhanced heat transfer and the pressure drop penalty. Ghani et al. [24] proposed a new configuration of MCHS with sinusoidal cavities and ribs, and investigated numerically its geometric parameters on hydrothermal performance. The results showed that the microchannel with relative cavity amplitude of 0.15, relative rib width of 0.3 and relative rib length of 0.5 yielded the best overall performance with $Pf = 1.85$ at $Re = 800$. Akbari et al.

[25] performed a numerical analysis of heat transfer and flow characteristics of MCHS with different rib height. They found that the heat transfer rate can be enhanced by increasing the rib height, volumetric percentage of nanoparticles and Reynolds number. However, the existence of ribs causes an increase in the average friction factor. Wang et al. [26] also conducted parameters optimization of the slant rectangular ribs in the MCHS by comprehensive consideration of heat transfer and pressure drop. The optimization results showed that the MCHS with the slant rectangular ribs have the best thermal performance with the attack angles of 52.5°, the relative height of 0.3, the relative length of 1 and the relative width of 0.1, respectively.

Many other researches are focused on the effect of rib's cross sectional shape on hydrothermal performance of MCHS. Chai et al. [27] studied numerically the heat transfer of the MCHS with rectangular, backward triangular, isosceles triangular, forward triangular and semicircular ribs. The results revealed that the forward triangular ribs can induce the largest Nusselt number in the microchannel. Meanwhile, the one with semicircular offset ribs brings about the best overall thermal performance. Moon et al. [28] also conducted a numerical investigation to analyze the effect of cross-sectional rib shapes on the heat transfer and friction loss performances. Among the considered sixteen rib shapes, the boot-shaped rib gave the best heat transfer performance with an average friction loss performance. Gholami et al. [29] investigated the effect of rectangular, oval, parabolic, triangular and trapezoidal ribs on the forced flow and heat transfer of the MCHS. The results indicated that the parabolic rib had the best proportion of Nusselt number enhancement comparing to the augmentation of the friction factor.

From the review of the available literature on thermal performance in the microchannel roughened with VRs and SRs, it is clear that VRs and SRs both can improve the heat transfer characteristic by disturbing the thermal boundary layers and inducing the recirculation for the mixing of hot and cold fluids. However, the disturbed thermal boundary layers and induced recirculation are only in the vertical or spanwise direction. Therefore, the heat transfer enhancement by the VRs and SRs is restricted in single direction, which is insufficient for improving the heat transfer ability of MCHS. In this paper, a new type of rib called "bidirectional rib (BR)", composed of VR and SR, is proposed to interrupt the thermal boundary layers and induce the recirculation in both vertical and

spanwise directions, and further intensify thermal transfer enhancement.

2. Problem statement and numerical methods

2.1. Physical models

A novel MCHS with BRs consists of two parts as shown in Fig. 1 (a): a cover with VR-roughened microchannels; a substrate with the SR-roughened microchannels. The VRs part contained in BRs are in-line distributed on the bottom surface of the cover and the SRs part are in staggered arrangement on the sidewalls. When the fluid flows through the BRs, the VRs part can improve the uniformity of the temperature and flow fields in the vertical direction. At the same time, the temperature and flow fields in the spanwise direction can be improved by the SRs part. The geometry dimension of the proposed MCHS with BRs is $21 \text{ mm} \times 11.9 \text{ mm} \times 1.5 \text{ mm}$ ($L \times W \times H$). The main structural parameters of the designed structure are shown in Table 1.

Considering that the designed MCHS is a periodic structure, only single-branch microchannel is selected as the computational domain to reflect the flow and heat transfer characteristics, as shown in Fig. 2(a). In order to study the effect of rib geometry on the fluid flow and heat transfer, other two relevant geometries, the microchannel only with VRs (VR-MC) and the microchannel only with SRs (SR-MC), are also considered in the present study, as shown in Fig. 2(b–c).

2.2. Governing equations and boundary conditions

The commercial FluentTM software is used to simulate the solid-fluid conjugate heat transfer process for different ribbed cases, which can provide us a convenient and precise method for

evaluating the heat transfer and flow characteristics. Meanwhile, the following assumptions are made to simplify the analysis: (1) Radiation, gravitational force, viscous dissipation and thermal contact resistance between components are neglected; (2) The solid and fluid properties are constant; (3) The fluid flow is steady and incompressible, and laminar flow prevails across the microchannels.

According to the aforesaid assumptions, the basic governing equations can be written as follows:

Continuity equation:

$$\nabla \cdot (\rho u) = 0 \quad (1)$$

Momentum equation:

$$(u \cdot \nabla) \rho u = -\nabla p + \mu \nabla^2 u \quad (2)$$

Energy equation:

$$u \cdot \nabla T = \frac{\lambda}{\rho C_p} \nabla^2 T \quad (3)$$

Energy equation in the solid domain is given by:

$$\lambda \nabla^2 T = 0 \quad (4)$$

where ρ is water density, u is the velocity at the inlet of the microchannel, p is pressure, C_p is the specific heat of the water, μ is the dynamic viscosity, and λ is the thermal conductivity of water.

The symmetric boundary conditions are applied onto the symmetric surface of model. Uniform velocity with different values and constant temperature ($T_{in} = 293 \text{ K}$) is applied in the inlet of the microchannel. At the exit, a pressure outlet boundary condition is specified with a fixed pressure of $1.013 \times 10^5 \text{ Pa}$. A uniform constant heat flux of $q = 100 \text{ W/cm}^2$ is applied on the top surface. The bottom surface has the assumed natural convection heat transfer

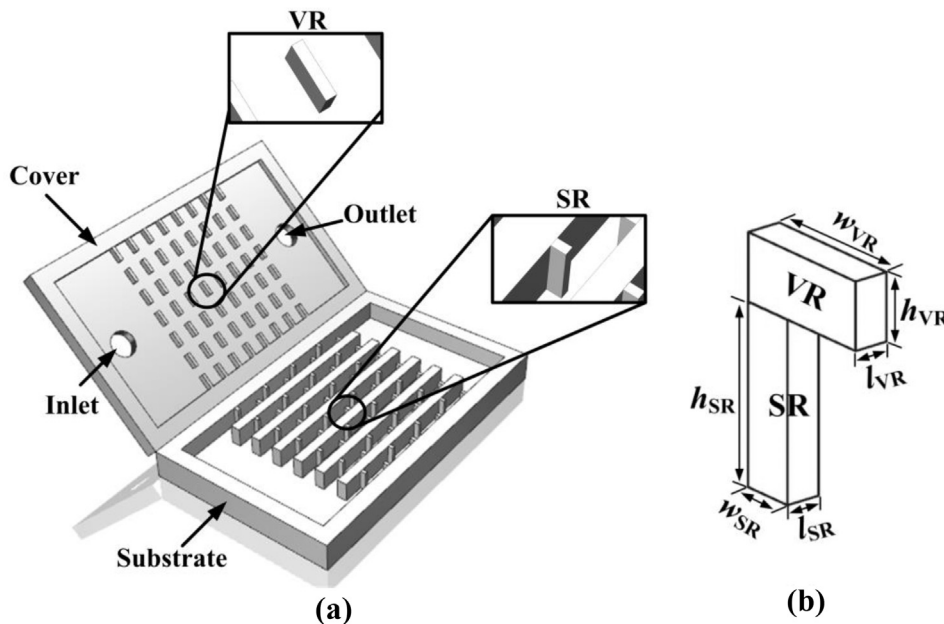


Fig. 1. Schematic of (a) the MCHS with BRs and (b) BR geometry.

Table 1
Microchannel geometry details.

Parameter	h_c	l_c	w_c	h_{VR}	w_{VR}	l_{VR}	h_{SR}	w_{SR}	l_{SR}	P	t_w
Values (μm)	500	10,000	450	150	450	100	350	150	100	1000	175

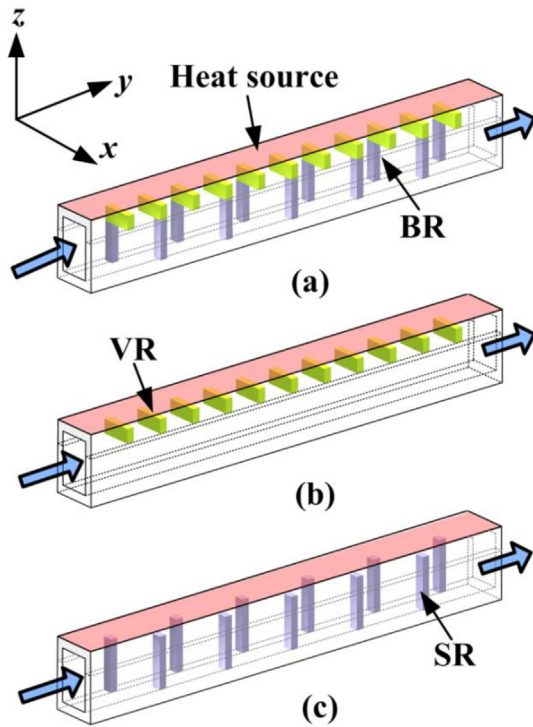


Fig. 2. Schematic of single-branch microchannels with (a) BRs, (b) VRs, and (c) SRs.

coefficient of $10 \text{ W/m}^2 \text{ K}$ since it is exposed in the air environment [30].

The aforesaid mass, momentum and energy governing equations are solved using the standard pressure and second-order upwind discretization scheme. The SIMPLE algorithm is employed for pressure velocity coupling to achieve the stability of solution convergence, and the convergence criteria of 10^{-6} for continuity and 10^{-8} for the energy equation are used in the numerical solution.

2.3. Grid independence study

To ensure the high accuracy of simulation results, every model adopts hexahedral elements generated by ANSYS ICEM CFD 14.5. As shown in the Fig. 3, fine mesh is concentrated near the wall region to resolve the large velocity gradient and thermal boundary layer, while the grid in the other parts is relatively sparse. To this end, the height of the first layer elements adjacent to the solid walls is set to be small enough to ensure a dimensionless wall distance (y^+) less than 1.0. To verify the mesh independence, four grid systems separately with 340,210 elements, 633,714 elements, 1,206,609 and 2,301,476 elements are generated in the BR-MC case and then the Nusselt number and friction factor are compared with different grid systems. The test results of the Nusselt number, friction factor and their relative error between the finest grids and other grids are shown in Table 2. It is found that the Nusselt number and friction factor with the third grid system differ from those with the fourth one by <0.5% and 0.4%, respectively. Therefore, considering the limitation of computation capability of the computer hardware, the third grid system with grid number of 1,206,609 is finally adopted for further simulation.

2.4. Data reduction

This section presents the relevant expressions which are used to calculate the heat transfer and fluid flow characteristics in MCHS.

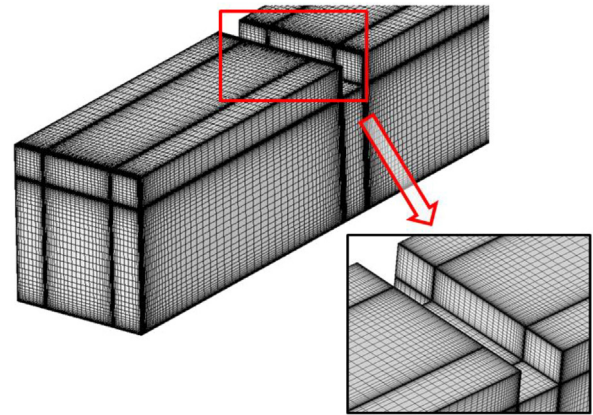


Fig. 3. The structured grid of ribbed passage in BR.

The Reynolds number (Re) is defined as:

$$Re = \rho \bar{u} D_h / \mu \quad (5)$$

where \bar{u} is mean velocity, D_h is the hydraulic diameter of the microchannel and it is calculated as:

$$D_h = 2w_c h_c / (w_c + h_c) \quad (6)$$

where w_c and h_c are width and height of microchannel, respectively.

The Fanning friction factor is used to evaluate the average friction factor of de-ionized (DI) water through the microchannels and its expression is given as:

$$f = \Delta p D_h / 2 \rho l_c \bar{u}^2 \quad (7)$$

where Δp and l_c are pressure drop across the microchannels and the total length of microchannels, respectively.

In experiment, the measured pressure drop of test device includes: the pressure drop across thirteen microchannels and the pressure losses owing to abrupt contraction and expansion at the inlet and outlet. Bucci *et al.* have reported an experimental method to obtain the pressure drop across microchannels [31]. According to their method, another MCHS with longer channel length of 20 mm and the same inlet and outlet manifolds was also manufactured. The pressure drop of two MCHS with channel length of 20 and 10 mm was tested under the same mass flow rate, respectively. Their difference was the pressure drop of 10 mm long microchannels without pressure losses at the inlet and outlet.

The thermal performance of the ribbed microchannels is evaluated in term of the average heat transfer coefficient and Nusselt number. They are defined as:

$$h = \frac{Q}{NA_{ch} \Delta T} = \frac{q A_{heat}}{2N(w_c + h_c) l_c \Delta T} \quad (8)$$

$$Nu = \frac{h D_h}{\lambda} \quad (9)$$

where Q is the total heat transfer, q is the heat flux, A_{heat} is heating area, A_{ch} is the contact surface area between the coolant and Si for single microchannel and ΔT is the mean temperature difference between the channel walls and the working fluid and its expression is given as:

$$\Delta T = T_w - (T_{in} + T_{out}) / 2 \quad (10)$$

where T_w , T_{in} and T_{out} are the mean temperature at the top surface of the Si covers, inlet and outlet temperature, respectively. The total heat carried away by the coolant can be determined from the following energy balance equation:

Table 2

The Nusselt number, friction factor and their relative error of the BR-MC with different grids at $Re = 100$.

Grids	340,210	633,714	1,206,609	2,301,476
Nusselt number	3.97	4.20	4.22	4.24
Relative error	1.7%	1.0%	0.5%	0
Friction factor	0.663	0.67	0.675	0.678
Relative error	2.3%	1.2%	0.4%	0

$$Q = \dot{m}C_p(T_{out} - T_{in}) \quad (11)$$

To prevent the heat losses at the inlet and outlet manifold, a layer of epoxy resin ($\lambda = 0.2 \text{ W/m/K}$) is coated on the inner and outer walls of inlet and outlet manifold.

The local Nusselts number at a fixed x is defined as:

$$Nu_x = \frac{qAD_h}{k_f A_c (T_{wx} - T_{wf})} \quad (12)$$

where T_{wx} and T_{fx} are the average temperature of wall and fluid at a fixed x , respectively.

For general evaluation of thermal and flow performance for different ribbed microchannels, the extensively used thermal performance factor is adopted. It can be written as:

$$\eta = \frac{Nu/Nu_s}{(f/f_s)^{1/3}} \quad (13)$$

where Nu_s and f_s are the Nusselt number and friction factor of the smooth microchannel, respectively.

3. Experiment

3.1. Fabrication

The designed MCHS with BRs was fabricated by micromachining technology. The main process procedure is schematically shown in Fig. 4 and described as follows:

- (a) To ensure the electrical insulation of the cover, a $2 \mu\text{m}$ thick SiO_2 was grown on both sides of a bare n-type (1 0 0) Si wafer with a thickness of $500 \mu\text{m}$.
- (b) A layer of photoresist (AZ P4620) was spun-coating on the back side of the wafer and then patterned by UV lithographic process.
- (c) The partial microchannels in the cover and VRs part in the BR were created by the inductively coupled plasma-reactive ion etching (ICP-RIE) process. Then the photoresist and the SiO_2 on the back side were removed using acetone solution and RIE process, respectively. The scanning electron micrograph (SEM) of the partial microchannels roughened with VRs is shown in Fig. 5(a).
- (d) Chromium/copper (Cr/Cu) seed layer was sputtered on the back side. After photoresist was spun-coating and patterned, a tin (Sn) layer was created on the two sides of the wafer by electroplate processes.
- (e) Another Cr/Cu seed layer was sputtered on the front side of the Si wafer. Subsequently, a nickel (Ni) thin-film heater as a heat source was created by the electroplating process. By aforesaid process, the cover with partial ribbed microchannels and heat source was completed.
- (f) Another Si wafer with thickness of 1 mm was processed to create the Si substrate with the rest SR-roughened microchannels. Firstly, a layer of photoresist was spin coated on the front side of the wafer, and then patterned by UV lithographic process to define the openings for the SRs and microchannels.

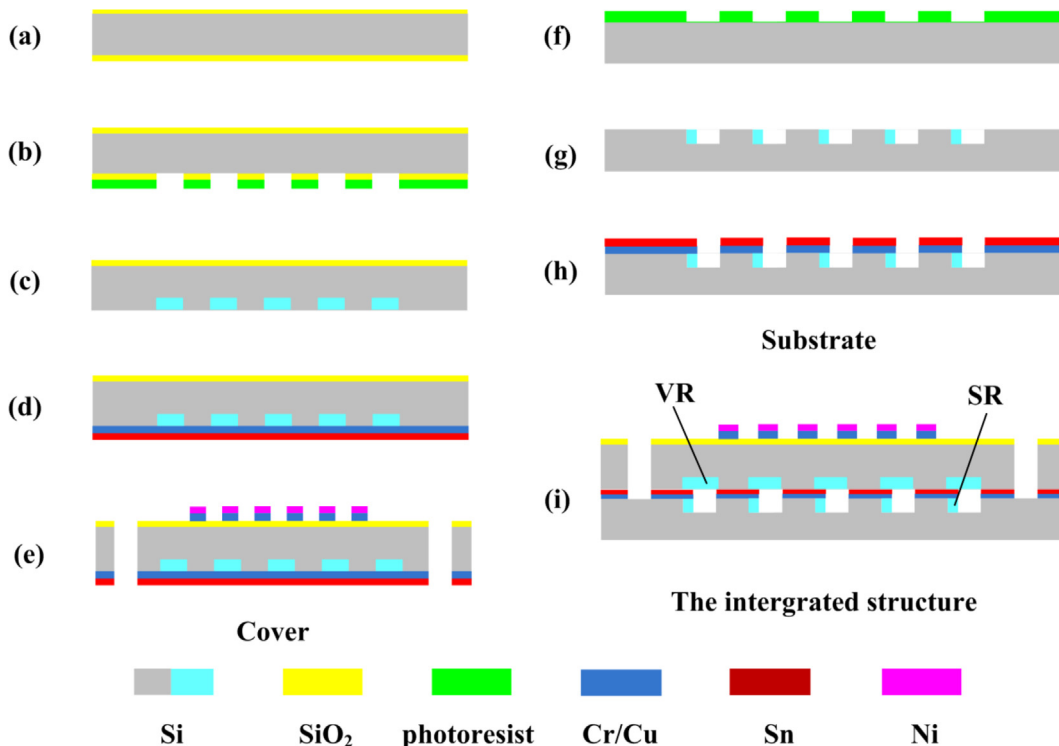


Fig. 4. The main fabrication process sketch of the MCHS with BRs.

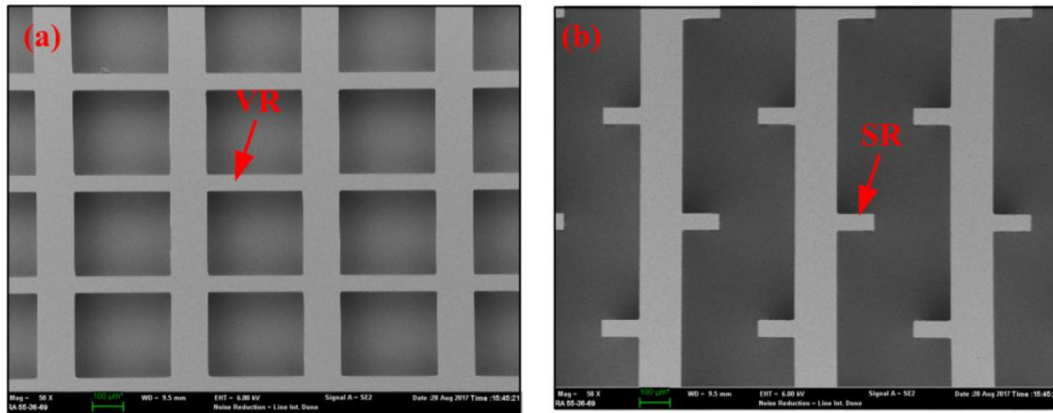


Fig. 5. The SEM of (a) the cover with VRs, (b) the substrate with SRs.

- (g) The ICP-RIE process was carried out to fabricate the SRs and the rest part of microchannels. Fig. 5(b) shows SRs and rest microchannels in the substrate.
- (h) A Sn layer was also created on the top side of the substrate by UV lithography and electroplate processes.
- (i) The prepared cover and substrate were then eutectically bonded together. They were assembled precisely by a Micro Placer (OK Industries MP-2000 Series@).

In order to compare the influence of BRs on the fluid flow and heat transfer, another two MCHS with VRs and SRs were also fabricated with same geometric dimensions and manufacturing processes.

3.2. Experimental setup

An experimental setup was designed to measure the heat transfer and friction characteristics of the MCHS with different ribs, as shown in Fig. 6. It was composed of a MASTERFLEX tubing pump, a filter, an electronic balance, two thermometers and piezometers, a DC power and an infrared thermal imager. In the experimental

tests, the DI water with constant temperature of 20 °C was selected as the working fluid. It was pumped by a MASTERFLEX tubing pump (made by Jasco, Model PU-2087 Plus, accuracy: $\pm 0.05\%$) from a reservoir and then purified by a filter (a membrane with a pore size of 0.2 μm) to remove the contaminants. The flow rate was controlled by the tubing pump and further affirmed by weighing the mass increment over a longer given period of time using a high precision electronic balance (made by Sartorius, Model TE214S, accuracy: ± 0.002 g). The measurements of temperature and pressure drop were carried out at the inlet and outlet by two thermometers and piezometers, respectively.

The Ni heater was connected to a precision DC power and the stable power input was controlled by adjusting applied current. The power input to the heaters was computed from the measurements of the current and the heater resistance. In order to prevent the heat loss at the inlet and outlet of manifolds, a layer of epoxy resin ($\lambda = 0.2$ W/m/K) was coated on their walls. The temperature distribution of top surface of the chip was captured by an infrared radiator imaging system (FLIR Thermal CAM PM595 IR). In order to keep a unified emissivity, a very thin uniform 'black lacquer' was sprayed on the chips' surface.

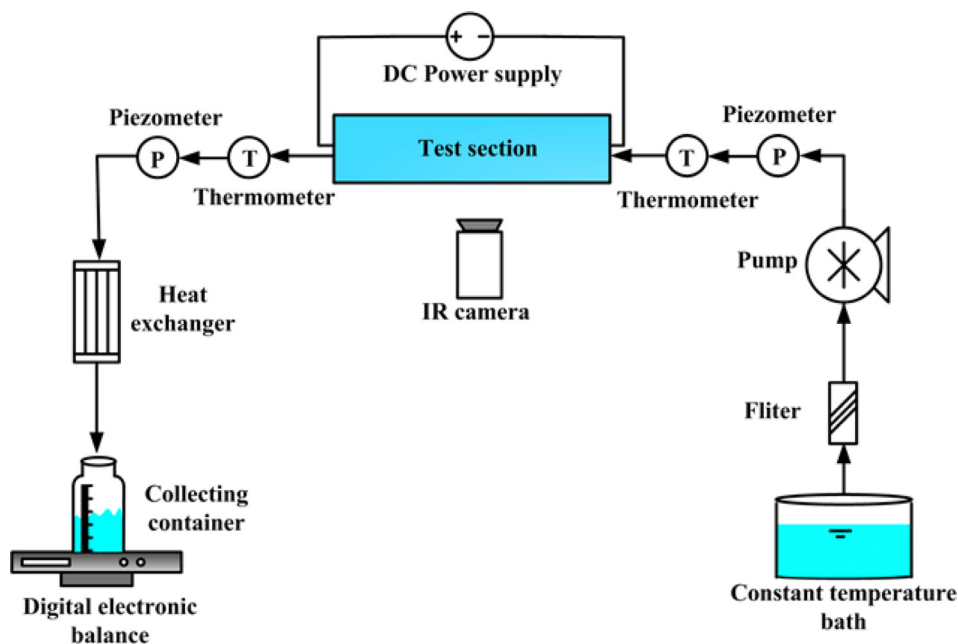


Fig. 6. Schematic of the experimental setup.

Table 3
Uncertainties for different parameters involved in the experimental tests.

Parameters	Uncertainty (%)	Parameters	Uncertainty (%)
D_h	0.69	Δp	0.98
A	0.1	Re	1.79
L	0.2	τ	2.1
$T_{out} - T_{in}$	2	Nu	4.89
T_{wall}	2	f	5.93
\dot{m}	0.98	η	6.75

3.3. Uncertainty analysis

An uncertainty analysis was carried out to give some quantitative description of the validity of test data. The uncertainties associated with direct measured parameters (W , H , L , T , P and \dot{m}) were obtained from the manufacturers' specification sheets. While the uncertainties of the calculated values (D_h , A , T_{out} , T_{in} , Δp , Re , Nu , f , τ and h) were determined using standard error analysis [32]. Their maximum uncertainties are all listed in Table 3.

4. Results and discussions

In this section, the average Nusselt numbers and apparent friction factor for all ribbed cases are measured and predicted with the Reynolds number varying from 100 to 1000. Detailed discussion has been provided for the mechanisms of different ribs on modification of heat transfer and flow characteristics. Thereafter, the effects of relative rib height of VR (e_{VR}) and relative rib width of SR (e_{SR}) on hydrothermal performance are elucidated.

4.1. Overall heat transfer and pressure drop characteristics

Fig. 7 shows the variation of average Nusselt number with Reynolds number for all ribbed microchannels. For all cases, the Nusselt number from the simulation and experiment matches each other well with a maximum deviation of 7.1%, 8% and 9.8% for BR-MC, VR-MC and SR-MC, respectively. With the rise of Reynolds number, the Nusselt number continuously increases since the heat transfer enhancement is amplified at high Reynolds numbers. In addition, BR-MC provides the higher Nusselt number values than VR-MC and SR-MC in the entire range of Reynolds number, while the ones of VR-MC yield the lowest. It is an indicator that the combined effect of VRs and SRs on heat transfer is better than individual effect in the microchannels. In addition, the difference between

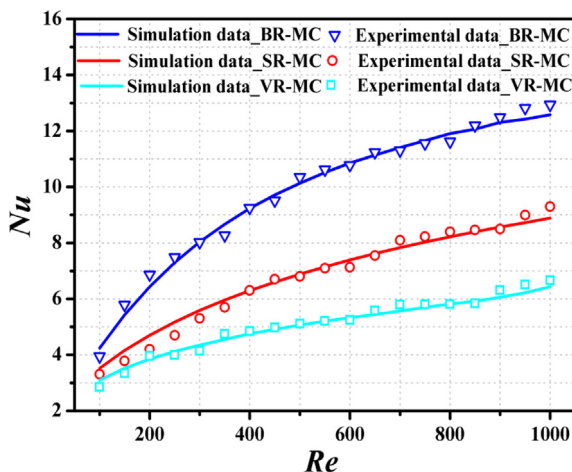


Fig. 7. The Nusselt number as a function of Reynolds number for all ribbed microchannels.

curves becomes larger with the increase of the Reynolds number. When $Re = 1000$, the Nusselt number of BR-MC can reach 1.95 and 1.42 times those of VR-MC and SR-MC, respectively. It can be interpreted that the higher flow rate can increase heat transfer enhancement, and two increments in BR-MC caused by the VR part and SP part are more than one in the VR-MC and SR-MC.

Fig. 8 shows the variation of Nu/Nu_0 with Reynolds number for SR-MC, VR-MC, BR-MC and the microchannel with forward triangular SR [27], where Nu_0 is the Nusselt number of the smooth microchannel. Chai et al. [27] investigated the laminar flow and heat transfer characteristics of the microchannels with five different SRs, including rectangular, backward triangular, isosceles triangular, forward triangular and semicircular ribs. Among the considered SRs in their study, forward triangular SR can provide the maximal Nu/Nu_0 in the microchannel, so the results of the microchannel with forward triangular SR are inserted in Fig. 8 for comparison. Apparently, the Nu/Nu_0 has the same trend with Nusselt number in Fig. 7. When $200 < Re < 850$, the Nu/Nu_0 of the SR-MCs is in the range of 1.5–1.86 and 1.48–1.71, respectively, which are approximate for all considered ribbed microchannels. Their difference is attributed to the different rib shapes and geometry dimensions. The proposed BR-MC yields the Nu/Nu_0 of 1.64–2.49, which are 0.21–0.61, 0.21–0.47, 0.37–1.05 times higher than the forward triangular SR, SR-MC and VR-MC, respectively. This indicates again the BR can provide the best effect on heat transfer enhancement.

The results above indicate that BR can induce the most prominent heat transfer enhancement in the microchannel with identical Reynolds number. However, it is considerable that the higher heat transfer enhancement is usually concerned with the penalty of increased apparent friction factor. Fig. 9 shows the variation of the apparent friction factor with Reynolds number for BR-MC, SR-MC and VR-MC. It is observed that the experimental results of the apparent friction factor are basically consistent with the numerical results, and their maximum deviation for BR-MC, VR-MC and SR-MC is 6.3%, 13.1% and 14.2%, respectively. Compared with SR-MC and VR-MC, the BR-MC provides a 51.6–80.7% and 58.2–89.3% higher apparent friction factor. Therefore, two components in BR, VR part and SP part, not only disturb the thermal boundary layer but also block fluid flow in both vertical and spanwise directions. In addition, the apparent friction factor all dramatically decreases with increasing of the Reynolds number for $Re < 300$ due to the suppression of the viscous sub-layer. When $Re > 300$, the rate of decreasing in the apparent friction factor is not distinct due to the prominent blocking effect of ribs.

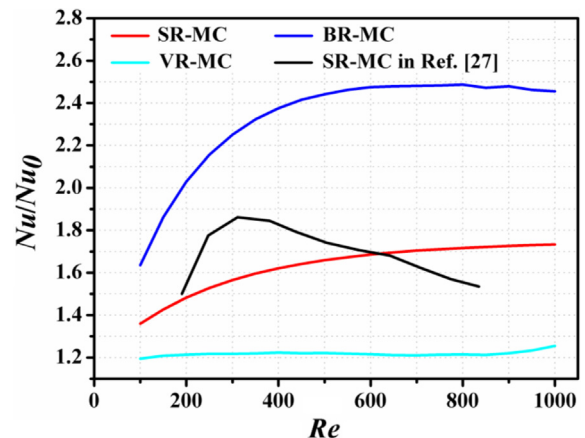


Fig. 8. The normalized Nusselt number as a function of Reynolds number for all ribbed microchannels.

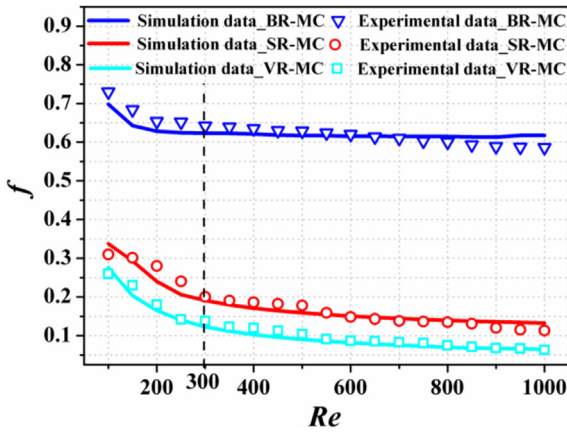


Fig. 9. The apparent friction factor as a function of Reynolds number for all ribbed microchannels.

4.2. Flow field and heat transfer mechanisms

In order to deeply understand the underlying mechanisms of the heat transfer and pressure drop characteristics among the three considered configurations, streamlines in the 3D microchannel model are presented and discussed in this section, as shown in

Fig. 10. When the fluid passes over the VRs in the microchannel, partial fluid is deflected to the vertical wall and then a large recirculation is created behind the VR, as shown in the Fig. 10(a). With the existence of the recirculation, the cold fluid at the center of microchannel is mixed with the hotter fluid closed to the vertical walls, which can produce a larger thermal difference between wall and coolant. At the same time, the thermal boundary layer closed to the vertical wall is disturbed and then redeveloped between the two adjacent VRs. However, the flow streamlines in the spanwise direction, except for the ones closing to the VR, are approximately paralleled with the streamwise. For SR-MC, the flow streamlines are forcing to deflect in the spanwise direction and recirculation is generated behind the SRs. Therefore, the interruption of thermal boundary layer and fluid mixing occur near the spanwise walls.

In comparison with the VR and SR, the BR provides a larger recirculation flow occupying most flow region in the microchannel, which indicates more cool fluid in the mainstream region is mixed with hotter fluid. As shown in the Fig. 10(c), it firstly flows towards the heating cover due to the VR part and then turns to the ribbed sidewall as result of SR part. The two deflections make the thermal boundary layers near the vertical and spanwise walls redevelop. Due to the successive distribution of the BRs, the thermal boundary layers will be interrupted again before they are fully developed. Thus, most thermal boundary layers in the BR-MC are in the developing state. This is main reason that the heat transfer efficiency of

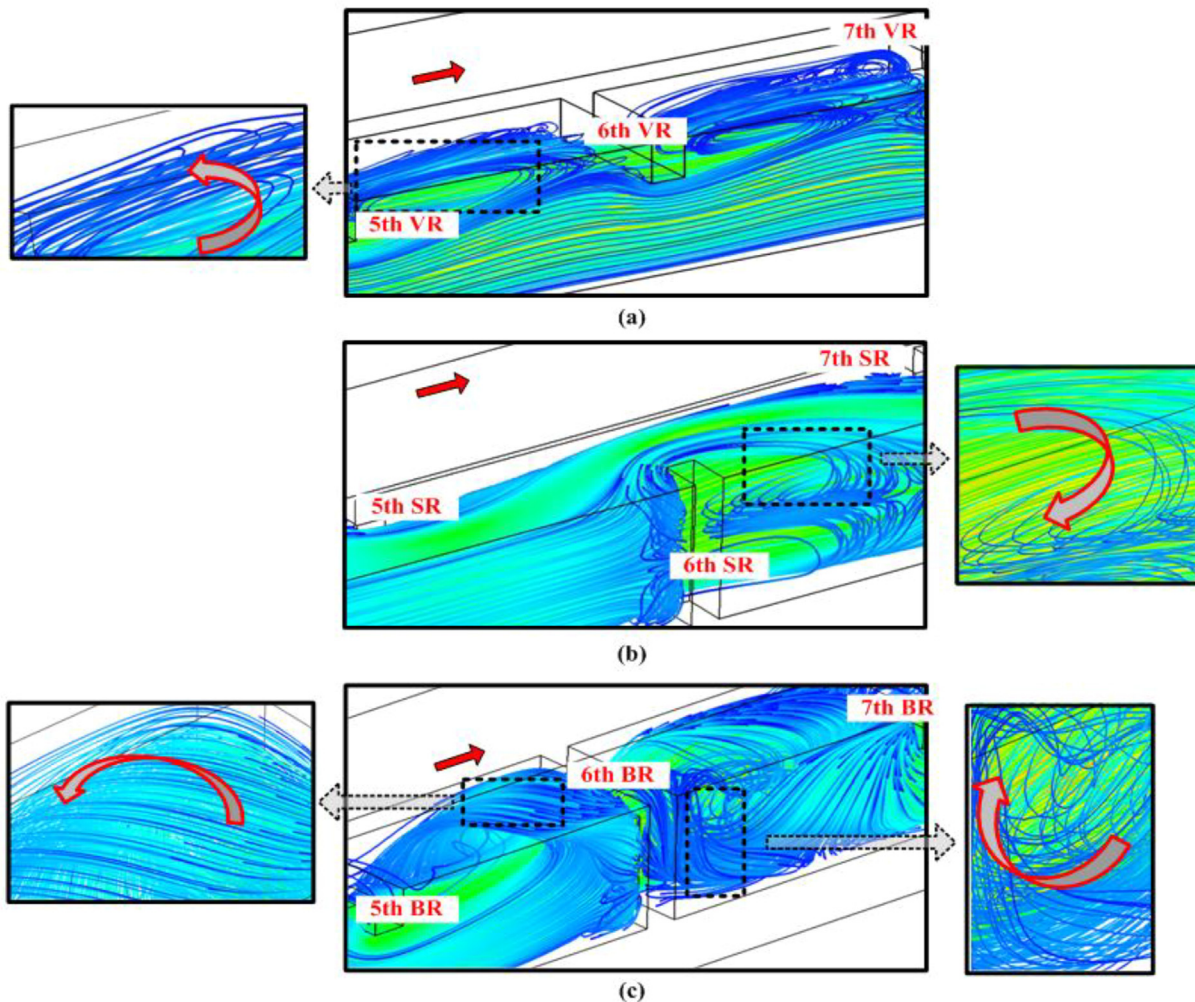


Fig. 10. Streamlines for microchannels with (a) VRs, (b) SRs and (c) BRs between the fifth and seventh ribs at $Re = 500$ in 3D microchannel structure.

BR-MC is better than those of VR-MC and SR-MC, shown in the Figs. 7 and 8.

Meanwhile, the 2D cross-sectional streamlines are also displayed to explore the flow field and heat transfer mechanisms. Fig. 11 displays the streamlines on the y - z cross section of $x = 0.3125$ mm (left) and x - y cross section of $z = 0.9$ mm (right) at $Re = 500$, selected between the fifth and sixth ribs of the test section. Apparently, the introduction of VR, SR and BR all induces recirculation flow in the microchannels. In Fig. 11(a), the VR can induce a large recirculation flow between two adjacent VRs on the y - z cross section, which disturbs the thermal boundary layer in vertical direction and causes the fluid under the cover exchanges with the mainstream. On the other x - y cross section, the streamlines are flat, which indicates no distinct secondary flow structure in the spanwise. On the contrary, the SRs can induce two recirculation flow on the x - y cross section, while there is no recirculation flow on the y - z cross section. As shown in Fig. 11(b), one small recirculation flow occurs at the leading bottom corner of the rib and the other large recirculation flow is located between the two adjacent ribs. Therefore, the VRs and SRs only generate recirculation flow and disturb the thermal boundary in the vertical and spanwise direction, respectively. However, no obvious flow structure change emerges in the other direction.

For BR-MC, recirculation flow can be observed on both y - z and x - y cross sections, as shown in Fig. 11(c). On the y - z cross section, two small recirculations are located on the trailing of VR and one relatively larger recirculation happens between two ribs. At the same time, a large scale recirculation flow and a small recirculation flow can be observed on the x - y cross section, and their positions and shapes are similar to those in the SR-MC. With the generated

recirculations in multi direction, the temperature field is more uniform and the temperature difference between the wall and coolant is smaller, which can improve convective heat transfer in the microchannel. However, owing to the bidirectional distribution of the BR, the cross-section area is larger than those of the SR-MC and VR-MC, which leads to a decrease in the flow area and thus a higher pressure drop.

Fig. 12 shows the detailed temperature field distribution between the fifth and sixth ribs on central cross sections ($x = 0.3125$ mm, $y = 5.55$ mm, $z = 0.9$ mm) for three ribbed microchannels at $Re = 500$. The temperature field distributions for all cases possess the same temperature level number. For VR-MC, as shown in Fig. 12(a), there exists obvious boundary between recirculation region and main stream. In the recirculation region, the temperature field presents uniform temperature and small gradient toward the heated cover due to the recirculation flow shown in Figs. 10(a) and 11(a). However, the thermal contour lines near the other walls are still dense. These imply that the VRs destroy the thermal boundary layer near the top wall and improve the temperature uniformity in the vertical direction. For SR-MC, in terms of temperature contour as revealed in Fig. 12(b), the temperature contour lines near the ribbed sidewalls are sparser compared with those close to the other walls. Therefore, the VRs and SRs only reduce the thermal boundary layer thickness in the corresponding ribbed direction. Compared with the VR-MC and SR-MC, the temperature contour lines in the BR-MC are sparse in the whole flow field and the temperature distribution is more uniform, as shown in Fig. 12(c). This indicates that the BRs can make the thermal boundary layer thinner in both vertical and spanwise direction and induce the greater temperature difference between walls and

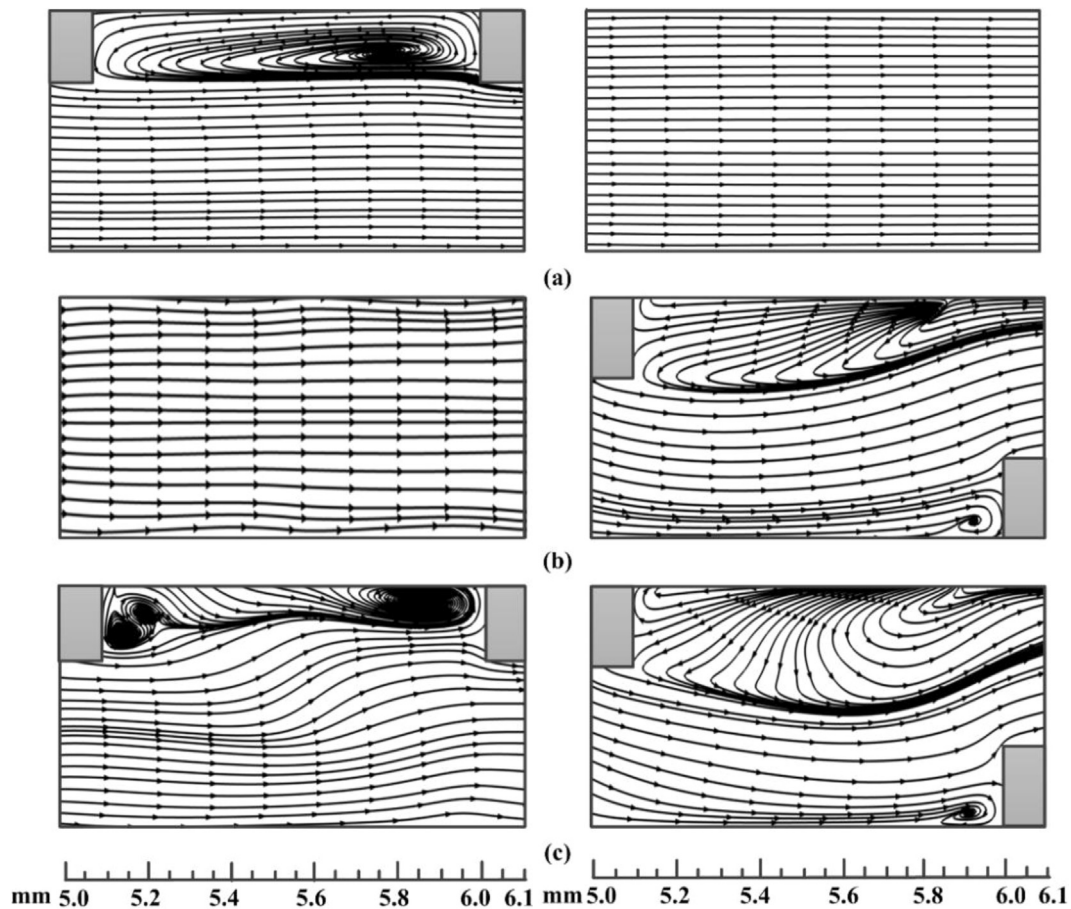


Fig. 11. Cross-sectional streamlines at $x = 0.3125$ mm (left) and $z = 0.9$ mm (right) between the fifth and sixth ribs for (a) VR-MC, (b) SR-MC and (c) BR-MC at $Re = 500$.

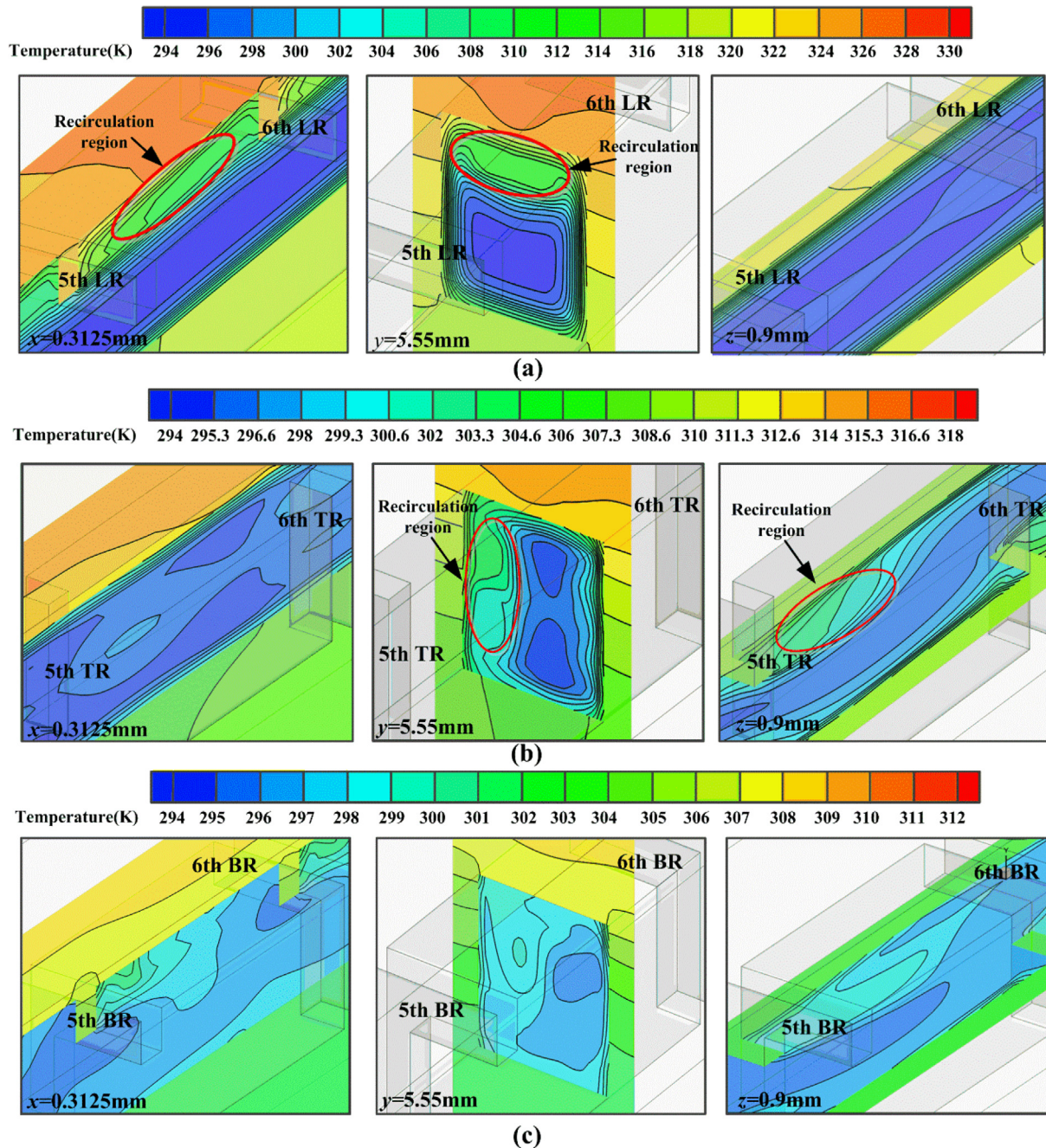


Fig. 12. Temperature field distribution between the fifth rib and sixth rib on center cross sections ($x = 0.3125\text{ mm}$, $y = 5.55\text{ mm}$, $z = 0.9\text{ mm}$) for (a) VR-MC, (b) SR-MC and (c) BR-MC at $Re = 500$.

coolant, which is advantageous to transport heat away from the wall and will bring about more heat transfer enhancement.

Heat transfer on the four walls of three ribbed microchannels has been demonstrated in terms of local Nusselt number (Nu_x), as shown in Fig. 13. Apparently, the local Nusselt numbers on four walls of three ribbed microchannels all display the cycle behavior between two adjacent ribs. Moreover, the local Nusselt numbers of BR-MC are all larger than those of the VR-MC and SR-MC. This indicates that the BRs provide the higher convective heat transfer enhancement as a result of the thinner thermal boundary layers, as observed in Fig. 12. For VR-MC and SR-MC, the periodic higher heat transfer appears at the leading of the ribs due to the impingement of coolant, while the deceleration downstream of the rib due to sudden expansion leads to a lower heat transfer on the trailing

of ribs. This trend is also observed for the BR-MC. In addition, a higher heat transfer in the BR-MC is observed on the non-ribbed sidewalls near the VR part, which is aroused by the impingement and acceleration of the flow, respectively.

4.3. Effects of relative rib height of VR (e_{VR}) and relative rib width of SR (e_{SR}) on hydrothermal performance

According to the prior results, it can be concluded that the BR-MC significantly outperforms VR-MC and SR-MC with respect to heat transfer performance. The next step of the present study is aimed at analyzing the effects of rib geometry on the thermal-hydraulic performance of BR-MC. The selected main geometry parameters, relative rib height of VR (e_{VR}) and relative rib width

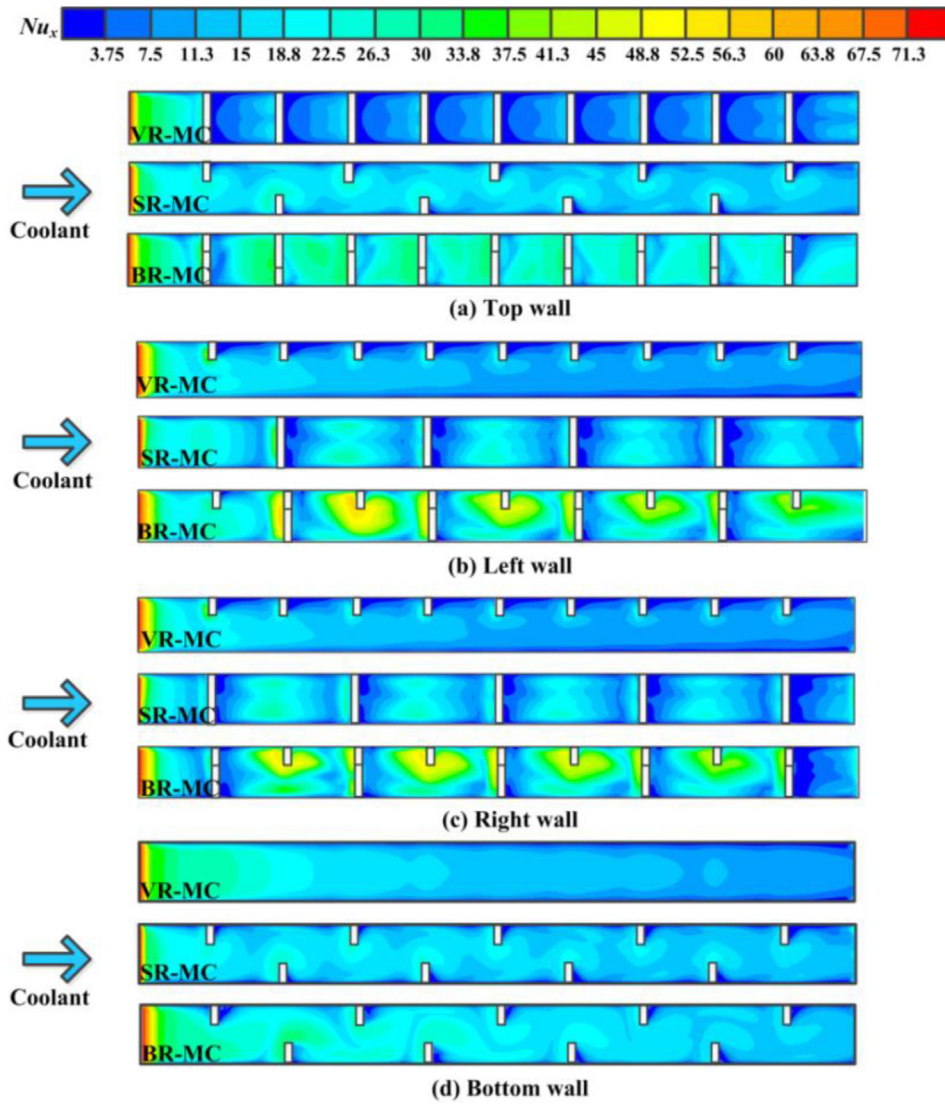


Fig. 13. Contours of local Nusselt number on (a) top wall, (b) left wall, (c) right wall and (d) bottom wall of the considered cases at $Re = 500$.

of SR (e_{SR}), are defined as the ratio of the VR height to the microchannel height ($e_{VR} = h_{VR}/h_c$) and the SR width to the microchannel width ($e_{SR} = w_{SR}/w_c$), respectively. The h_{VR} and w_{SR} are in the range of 0–200 μm , whereas the other geometric parameters of BR are kept constant as listed in Table 1.

Fig. 14 depicts the variation of Nusselt number with e_{SR} and e_{VR} for BR-MC at $Re = 500$. The figure shows that the Nusselt number both continuously increases with the increment of e_{SR} and e_{VR} . When $e_{SR} = 0.45$ and $e_{VR} = 0.4$, the Nusselt numbers can reach 12.05 and 11.88, respectively. With the larger e_{SR} and e_{VR} , the more volume of cooling fluid is involved in mixing in each redeveloping zone. Besides, the enlargement in e_{SR} and e_{VR} promotes jet impingement and enlarges the surface area. All these factors are contributing to the heat transfer enhancement. In addition, the results with $e_{SR} = 0$ and $e_{VR} = 0$ once again confirm that the BR can provide more sufficient heat transfer enhancement in comparison with SR and VR.

The effects of e_{SR} and e_{VR} on the apparent friction factor are seen from Fig. 15. It is obvious that the apparent friction factor both increases continuously with the increasing of e_{SR} and e_{VR} for the

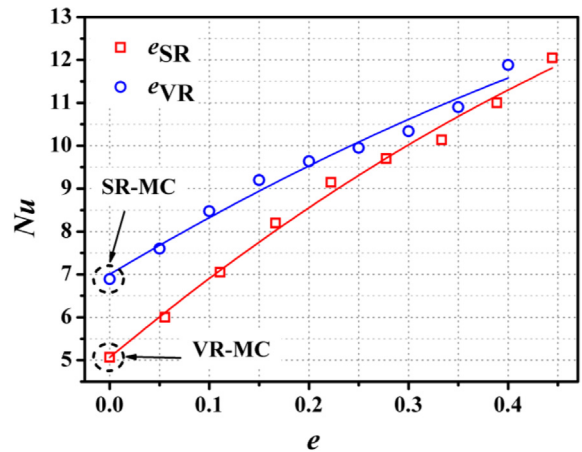


Fig. 14. Variation of average Nusselt number with e_{SR} and e_{VR} for BR-MC at $Re = 500$. (Correlation with e_{SR} : $Nu = 5.06648 + 19.29044e_{SR} - 9.25658e_{SR}^2$, error < 3.28%; correlation with e_{VR} : $Nu = 7.00058 + 13.83435e_{VR} - 5.96057e_{VR}^2$, error < 5.94%.)

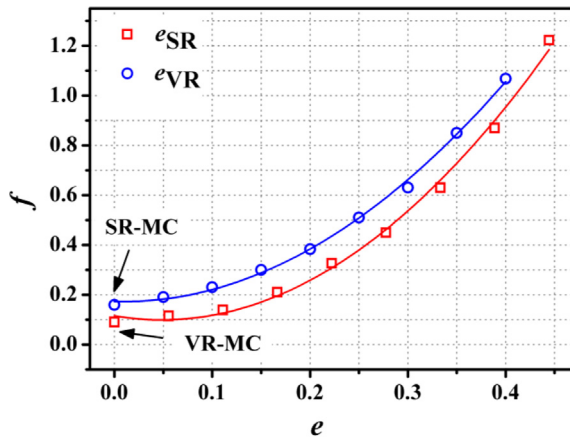


Fig. 15. Variation of average friction factor with e_{SR} and e_{VR} for BR-MC at $Re = 500$. (Correlation with e_{SR} : $f = 0.11544 - 0.67269e_{SR} + 6.92454e_{SR}^2$, error < 10.1%; correlation with e_{VR} : $f = 0.12525e_{VR}^{0.18815} + 0.02525$, error < 5.2%.)

entire Reynolds numbers. When $e_{SR} = 0.45$ and $e_{VR} = 0.4$, the apparent friction factor are 13.6 and 6.6 times of the ones at $e_{SR} = 0$ and $e_{VR} = 0$, respectively. According to the Fig. 9, the reduction of cross-section area of fluid flow leads to an increment of apparent friction factor. Similarly, the increasing of e_{SR} and e_{VR} also make the cross-section area shrink and then block the fluid flow. This is the reason that the pressure drop significantly increases with the increment of the e_{SR} and e_{VR} . Therefore, the e_{SR} and e_{VR} cannot be too large because they will induce much more pressure drop and weaken the thermal performance. According to the results with $e_{SR} = 0$ and $e_{VR} = 0$, it is proved that the apparent friction factor in the BR-MC is higher than SR-MC and VR-MC as result of the combined barrier effect of SR and VR in the microchannel.

Fig. 16 shows the thermal enhancement factor as a function of e_{SR} and e_{VR} for BR-MC at $Re = 500$. The thermal enhancement factor firstly increases dramatically and then decreases as e_{SR} and e_{VR} increase. The $e_{VR} = 0.15$ and $e_{SR} = 0.17$ introduce the maximal thermal enhancement factor of 1.19 and 1.16, respectively. When $e_{VR} < 0.316$ and $0.026 < e_{SR} < 0.357$, the thermal enhancement factor is all larger than unity. This implies that the BR-MC possess high heat transfer enhancement which can offset the pressure drop penalties caused by the BRs. While the thermal enhancement factor is smaller than unity when $e_{VR} > 0.316$ and $e_{SR} > 0.357$. This is because the increase of e_{VR} and e_{SR} causes a more significant increment in the pressure drop penalty than the heat transfer enhancement. Owing to the serious pressure drop, the BR-MC loses its advantages as an effective heat transfer enhancement method.

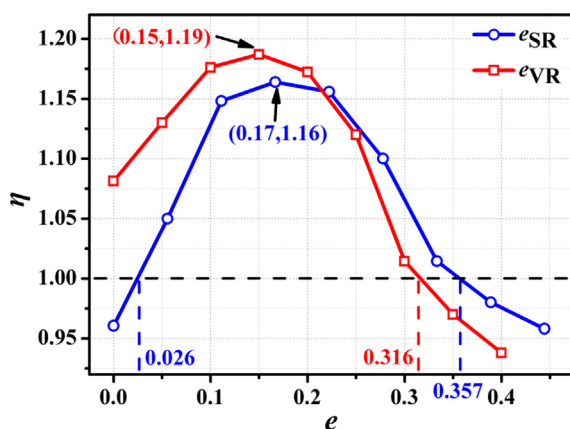


Fig. 16. The thermal enhancement factor as a function of e_{SR} and e_{VR} at $Re = 500$.

5. Conclusion

The hydrothermal performance of MCHS with BRs has been studied experimentally and numerically, and compared with those with relevant rib geometries such as VRs and SRs. Mechanisms underlying the heat transfer enhancement by BRs are clarified in detail. Furthermore, the effects of e_{VR} and e_{SR} on heat transfer and flow performance are discussed. The main conclusions can be made as follows:

- (1) With the same mass flow rate, the Nusselt number of the BR-MC is nearly 1.2–1.42 times and 1.4–2 times those of VR-MC and SR-MC, which means that the heat transfer enhancement ability of BR is better than VR and SR.
- (2) For all ribbed microchannels, the apparent friction factor all increases with the rise of Reynolds number. The utilizing of the BRs in the microchannel causes the highest apparent friction factor which attributes to the more prominent blocking effect.
- (3) The BRs provide the higher heat transfer by interrupting thermal boundary layer and inducing the recirculation in both vertical and spanwise directions. Therefore, the local Nusselt number of four walls in BR-MC is kept to be highest.
- (4) For BR-MC, the rises of e_{VR} and e_{SR} both can improve the heat transfer but increase the apparent friction factor. Taking the heat transfer and pressure drop into account concurrently, the BRs with $e_{VR} < 0.316$ and $0.026 < e_{SR} < 0.357$ can provide the thermal enhancement factor values above than 1.

Conflict of interest

The authors declared that there is no conflict of interest.

Acknowledgements

This research has been sponsored by the Young Foundation of Shanghai, China (ZZGCD16004), the National Natural Science Foundation of China (No. 51605277, No. 61803254 and No. 61601296).

References

- [1] G. Wang, D. Niu, F. Xie, Y. Wang, X. Zhao, G. Ding, Experimental and numerical investigation of a microchannel heat sink (MCHS) with micro-scale ribs and grooves for chip cooling, *Appl. Therm. Eng.* 85 (2015) 61–70.
- [2] C. Mira-Hernandez, M.D. Clark, J.A. Weibel, S.V. Garimella, Development and validation of a semi-empirical model for two-phase heat transfer from arrays of impinging jets, *Int. J. Heat Mass Transf.* 124 (2018) 782–793.
- [3] D.Y. Yeo, H.C. No, Modeling film boiling within chimney-structured porous media and heat pipes, *Int. J. Heat Mass Transf.* 124 (2018) 576–585.
- [4] S.P. Aly, A.F.M. Arif, K.S. Al-Athel, J. Mostaghimi, S.M. Zubair, Performance of open pore metal foam heat sinks fabricated with thermally sprayed interface, *Appl. Therm. Eng.* 105 (2016) 411–424.
- [5] Y.M. Yu, T.W. Simon, M. Zhang, T. Yeom, M.T. North, T.H. Cui, Enhancing heat transfer in air-cooled heat sinks using piezoelectrically-driven agitators and synthetic jets, *Int. J. Heat Mass Transf.* 68 (2014) 184–193.
- [6] A. Ghahremanzhad, K. Vafai, Thermal and hydraulic performance enhancement of microchannel heat sinks utilizing porous substrates, *Int. J. Heat Mass Transf.* 122 (2018) 1313–1326.
- [7] T.M. Harms, M.J. Kazmierczak, F.M. Gerner, Developing convective heat transfer in deep rectangular microchannels, *Int. J. Heat Fluid Flow* 20 (2) (1999) 149–157.
- [8] S. Lu, A comparative analysis of innovative microchannel heat sinks for electronic cooling, *Int. Commun. Heat Mass Transf.* 76 (2016) 271–284.
- [9] J. Ryu, D.H. Choi, S.J. Kim, Numerical optimization of the thermal performance of a microchannel heat sink, *Int. J. Heat Mass Transf.* 45 (13) (2002) 2823–2827.
- [10] C.J. Ho, P.-C. Chang, W.-M. Yan, P. Amani, Thermal and hydrodynamic characteristics of divergent rectangular minichannel heat sinks, *Int. J. Heat Mass Transf.* 122 (2018) 264–274.
- [11] Z. Yang, J. Shi, J. Yao, X. Zhang, G. Ding, X. Zhao, A laterally driven MEMS inertial switch with double-layer suspended springs for improving single-axis sensitivity, *IEEE Trans. Compon. Packag. Manuf. Technol.* 8 (10) (2018) 1845–1854.

- [12] D.B. Tuckerman, R.F. Pease, High-performance heat sinking for VLSI, *IEEE Electron Device Lett.* 2 (5) (1981) 126–129.
- [13] A.A.A. Arani, O.A. Akbari, M.R. Safaei, A. Marzban, A.A.A.A. Alrashed, G.R. Ahmadi, T.K. Nguyen, Heat transfer improvement of water/single-wall carbon nanotubes (SWCNT) nanofluid in a novel design of a truncated double-layered microchannel heat sink, *Int. J. Heat Mass Transf.* 113 (2017) 780–795.
- [14] T.-C. Hung, Y.-X. Huang, W.-M. Yan, Thermal performance analysis of porous-microchannel heat sinks with different configuration designs, *Int. J. Heat Mass Transf.* 66 (2013) 235–243.
- [15] J.L. Xu, Y.H. Gan, D.C. Zhang, X.H. Li, Microscale heat transfer enhancement using thermal boundary layer redeveloping concept, *Int. J. Heat Mass Transf.* 48 (9) (2005) 1662–1674.
- [16] L. Chai, G. Xia, L. Wang, M. Zhou, Z. Cui, Heat transfer enhancement in microchannel heat sinks with periodic expansion–contraction cross-sections, *Int. J. Heat Mass Transf.* 62 (2013) 741–751.
- [17] H. Shafeie, O. Abouali, K. Jafarpur, G. Ahmadi, Numerical study of heat transfer performance of single-phase heat sinks with micro pin-fin structures, *Appl. Therm. Eng.* 58 (1–2) (2013) 68–76.
- [18] H.E. Ahmed, M.I. Ahmed, Optimum thermal design of triangular, trapezoidal and rectangular grooved microchannel heat sinks, *Int. Commun. Heat Mass Transf.* 66 (2015) 47–57.
- [19] L. Chai, G. Xia, M. Zhou, J. Li, J. Qi, Optimum thermal design of interrupted microchannel heat sink with rectangular ribs in the transverse microchambers, *Appl. Therm. Eng.* 51 (1–2) (2013) 880–889.
- [20] T. Desrues, P. Marty, J.F. Fourmigué, Numerical prediction of heat transfer and pressure drop in three-dimensional channels with alternated opposed ribs, *Appl. Therm. Eng.* 45–46 (2012) 52–63.
- [21] G. Jiang, X. Shi, G. Chen, J. Gao, Study on flow and heat transfer characteristics of the mist/steam two-phase flow in rectangular channels with 60 deg. ribs, *Int. J. Heat Mass Transf.* 120 (2018) 1101–1117.
- [22] G. Xie, X. Liu, H. Yan, J. Qin, Turbulent flow characteristics and heat transfer enhancement in a square channel with various crescent ribs on one wall, *Int. J. Heat Mass Transf.* 115 (2017) 283–295.
- [23] G. Xia, Y. Zhai, Z. Cui, Numerical investigation of thermal enhancement in a micro heat sink with fan-shaped reentrant cavities and internal ribs, *Appl. Therm. Eng.* 58 (1–2) (2013) 52–60.
- [24] I.A. Ghani, N. Kamaruzaman, N.A.C. Sidik, Heat transfer augmentation in a microchannel heat sink with sinusoidal cavities and rectangular ribs, *Int. J. Heat Mass Transf.* 108 (2017) 1969–1981.
- [25] O.A. Akbari, D. Toghraie, A. Karimipour, M.R. Safaei, M. Goodarzi, H. Alipour, M. Dahari, Investigation of rib's height effect on heat transfer and flow parameters of laminar water–Al₂O₃ nanofluid in a rib-microchannel, *Appl. Math. Comput.* 290 (2016) 135–153.
- [26] R.-J. Wang, J.-W. Wang, B.-Q. Lijin, Z.-F. Zhu, Parameterization investigation on the microchannel heat sink with slant rectangular ribs by numerical simulation, *Appl. Therm. Eng.* 133 (2018) 428–438.
- [27] L. Chai, G.D. Xia, H.S. Wang, Numerical study of laminar flow and heat transfer in microchannel heat sink with offset ribs on sidewalls, *Appl. Therm. Eng.* 92 (2016) 32–41.
- [28] M.-A. Moon, M.-J. Park, K.-Y. Kim, Evaluation of heat transfer performances of various rib shapes, *Int. J. Heat Mass Transf.* 71 (2014) 275–284.
- [29] M.R. Gholami, O.A. Akbari, A. Marzban, D. Toghraie, G.A.S. Shabani, M. Zarringhalam, The effect of rib shape on the behavior of laminar flow of oil/MWCNT nanofluid in a rectangular microchannel, *J. Therm. Anal. Calorim.* 134 (3) (2017) 1611–1628.
- [30] R. Zhao, L. Gosselin, M. Fafard, D.P. Ziegler, Heat transfer in upper part of electrolytic cells: Thermal circuit and sensitivity analysis, *Appl. Therm. Eng.* 54 (1) (2013) 212–225.
- [31] A. Bucci, G.P. Celata, M. Cumo, E. Serra, G. Zummo, Water single-phase fluid flow and heat transfer in capillary tubes, *Therm. Sci. Eng.* 11 (6) (2003) 319–326.
- [32] J.R. Taylor, W.J. Thompson, An introduction to error analysis: the study of uncertainties in physical measurements, *Phys. Today* 51 (1) (1998) 57–58.